Anomalous nonequilibrium phonon scattering in the Weyl semimetal WP_2

Junhong Yu,[1,*] Jianzhou Zhao,[2,*] Yangyang Lv,[3,*] Yadong Han,[1,4] Zhang Hang,[1,4] Jinlong Xu,[3,†] and Jianbo Hu[1,4,‡]

[1]*Laboratory for Shock Wave and Detonation Physics, Institute of Fluid Physics, China Academy of Engineering Physics, Mianyang 621900, China*

[2]*Co-Innovation Center for New Energetic Materials, Southwest University of Science and Technology, Mianyang 621010, China*

[3]*National Laboratory of Solid State Microstructures, School of Electronic Science and Engineering, School of Physics, Nanjing University, Nanjing 210093, China*

[4]*State Key Laboratory for Environment-Friendly Energy Materials, Southwest University of Science and Technology, Mianyang 621010, China*

(Received 4 October 2022; accepted 2 May 2023; published 30 May 2023)

The type-II Weyl semimetal (WSM) β-WP_2 was recently demonstrated as a supreme quantum material with various interestingtransport properties. Toward deciphering these peculiar transport phenomena for future topological device applications, it is highly necessary to understand the dynamical process of phonon scatterings under nonequilibrium conditions. By performing temperature-dependent coherent phonon spectroscopy in β-WP_2, we provide here direct experimental evidence that phonons decaying into electron-hole pairs overwhelm the anharmonic phonon-phonon scattering process. Remarkably, the dominating phonon-electron coupling in β-WP_2 is further supported by observations of the transient Fano resonance. First-principles calculations suggest that the anomalous phonon decaying results from the acoustic bunching and the limited phonon density of states in β-WP_2. Our real-time observations provide dynamical insight into quasiparticle scatterings that are of vital importance for fundamental transport properties in β-WP_2.

DOI: 10.1103/PhysRevResearch.5.023137

I. INTRODUCTION

Topological semimetals offer excellent material platforms for the design of solid-state devices thanks to their exotic physical properties such as the anomalous Hall effect, large magnetoresistance, and high carrier mobilities [1–5]. Among the few topological semimetals that have been discovered, the transition metal diphosphide β-WP_2 is a confirmed nonlayered type-II Weyl semimetal, which supports simple band structure [6,7] and robust Weyl points against structural distortions [6,8], hence attracting enormous attention in condensed matter physics. More interestingly, static thermal and electrical measurements recently demonstrated that β-WP_2 single crystals exhibit hydrodynamic electron transport (i.e., in contrast to the ohmic electron transport in ordinary metals) and violate the Wiedemann-Franz (WF) law in thermal transport down to 5 K [9–11]. This observation raises fundamental questions regarding the relevance of quasiparticle scattering processes to this nontrivial transport phenomenon.

Phonons, the fundamental vibrational modes of a crystal lattice, play critical roles in determining both thermal (e.g., thermal conductivity is depending on the anharmonic phonon-phonon scatterings) [12,13] and electrical (e.g., electrical conductivity is affected by electron scatterings with optical phonons) [14] properties. It is thus speculated that the observed exotic transport might be linked to the unusual phonon scattering processes in β-WP_2. Following this thought, previous computational works have suggested the importance of electron-phonon coupling in understanding the macroscopic transport properties of β-WP_2 [15]. Unfortunately, experimental evaluation of microscopic dynamics of phonon scatterings in β-WP_2 has been elusive despite that recent continuous-wave Raman measurements have roughly estimated the optical decay rate based on the Raman spectra linewidths [16–18]. Up to now, direct and unambiguously experimental evidence is still lacking to validate the importance of phonon scattering in understanding the anomalous transport properties in β-WP_2.

To fill in this gap, we have performed femtosecond-resolved coherent phonon spectroscopy to investigate the dynamic phonon scattering process in β-WP_2. A remarkable finding is that coherent phonons in β-WP_2 tend to decay by scattering off electrons (i.e., decay into electron-hole pairs) rather than—as in conventional materials—by scattering off other phonons (i.e., decay into acoustic phonons) [19]. In addition, a transient (persisting up to ∼1 ps after photoexcitation) Fano resonance [20,21], which originates from strong coupling between discrete phonons and continuous electron-hole pair excitations, further supports the dominating

*These authors contributed equally to this paper.
†Author to whom correspondence should be addressed: longno.2@163.com
‡Author to whom correspondence should be addressed: jianbo.hu@caep.cn

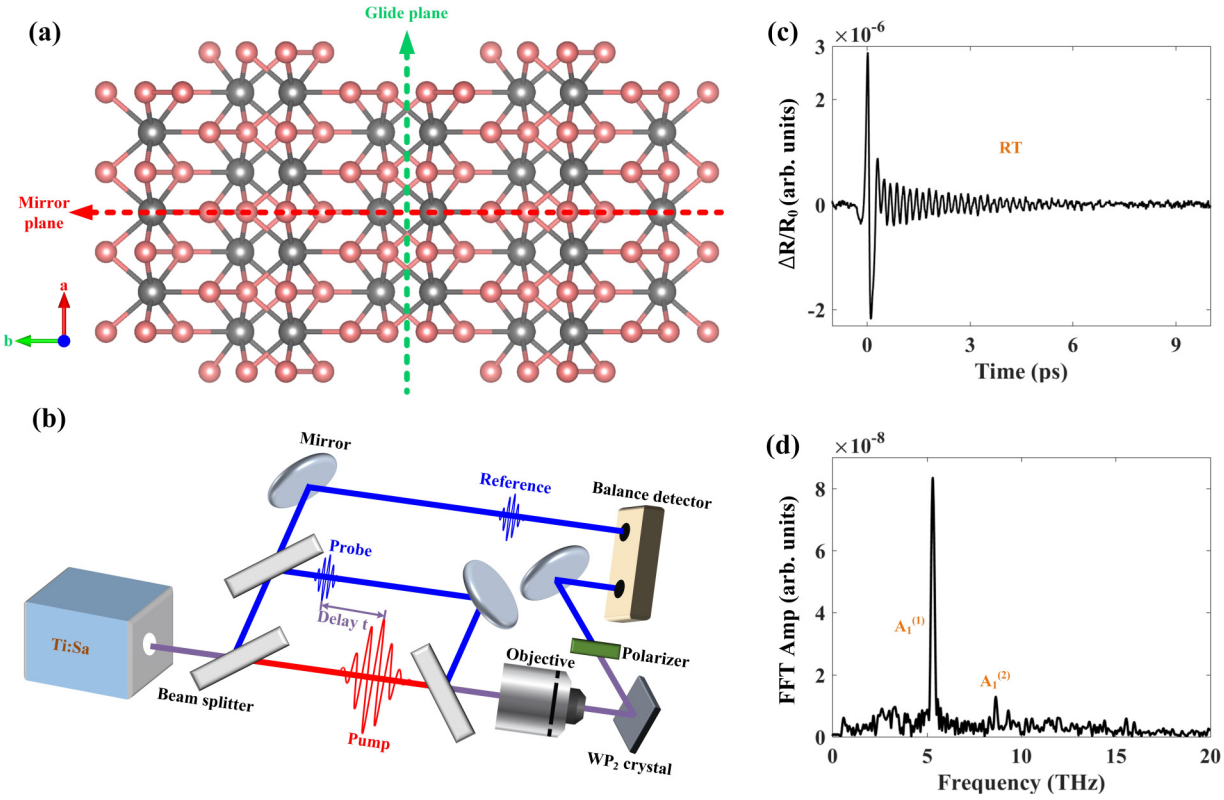

FIG. 1. Crystal structure and room-temperature coherent phonon spectra of β-WP_2. (a) Crystal structure of β-WP_2. The W and P atoms are denoted by the light black and red spheres, respectively. The glide and mirror planes are also indicted. (b) Schematic experimental setup of the ultrafast coherent phonon spectroscopy. (c) Time-domain lattice vibrations in β-WP_2 at room temperature (RT). Please note that the excited carrier response has been subtracted. (d) FT spectrum of the time-domain lattice vibrations showing the two lowest-energy A_1 optical phonon modes at ~5.05 and ~8.58 THz. Please note that the coherent phonon linewidth in the nonequilibrium measurement is typically larger than that in the static Raman measurement [18], which is due to the transient temperature rise, transient depopulation, and transient dephasing process with the ultrafast laser pulse excitation [26].

phonon-electron scattering scenario in β-WP_2. In conjunction with first-principles calculations, we argue that with such an anomalous phonon-electron scattering picture, electrons and phonons may become coupled, forming quasiparticles and inducing unusual transport properties in β-WP_2.

II. RESULTS AND DISCUSSION

The high-quality β-WP_2 crystal with shiny surfaces was prepared by a chemical vapor transport (CVT) technique following the reported methods [16,22]. Details of the crystal growth process and confirmations of the β phase can be found in our previous publication [23]. As shown in Fig. 1(a), β-WP_2 is demonstrated to crystallize in the space group of $Cmc2_1$ and has a noncentrosymmetric structure with a glide plane perpendicular to the b axis, and a mirror plane perpendicular to the a axis [16,24,25]. The orthorhombic, nonsymmorphic space group $Cmc2_1$ belongs to the C_{2v} point group and leads to a total of 18 phonon modes, in which 15 optical modes ($5A_1 + 3A_2 + 2B_1 + 5B_2$) are all Raman active and have been detected in the equilibrium Raman spectroscopy [16–18]. Figure 1(b) presents a schematic of the femtosecond-resolved coherent phonon spectroscopy, allowing us to directly monitor nonequilibrium lattice vibrations in the time domain [26–30]. Briefly, an 800-nm pump pulse with a pulse duration of 20 fs and a fluence of ~5 $\mu J/cm^2$ promotes β-WP_2 (the direct band gap: 0.6–0.8 eV [23]) into the excited state and generates coherent atomic motions via the displacive excitation mechanism [28], which is then detected by an 800-nm probe pulse with the same pulse duration and an order of magnitude weaker fluence (more experimental details are provided in Appendix A).

Figure 1(c) shows a typical time-domain signal measured at room temperature after removing the nonoscillation signal related to photoexcited carriers by exponential fittings convoluted with the instrumental response function [27–30] and frequencies of coherent phonon modes can be clarified from Fourier transform (FT) of the time domain oscillatory pattern. Due to the isotropic detection scheme [31], only five A_1 Raman-active phonon modes can be observed based on the relationship among Raman tensors, polarizations of the pump, and probe pulses [16]. As shown in Fig. 1(d), the FT spectrum reveals two lattice modes at ~5.05 and ~8.58 THz, the frequencies of which are in good agreement with previously reported Raman experiments [16–18] and thus can be assigned as the two lowest-energy A_1 phonon modes ($A_1^{(1)}$ and $A_1^{(2)}$). The absence of other high-order A_1 phonon modes in

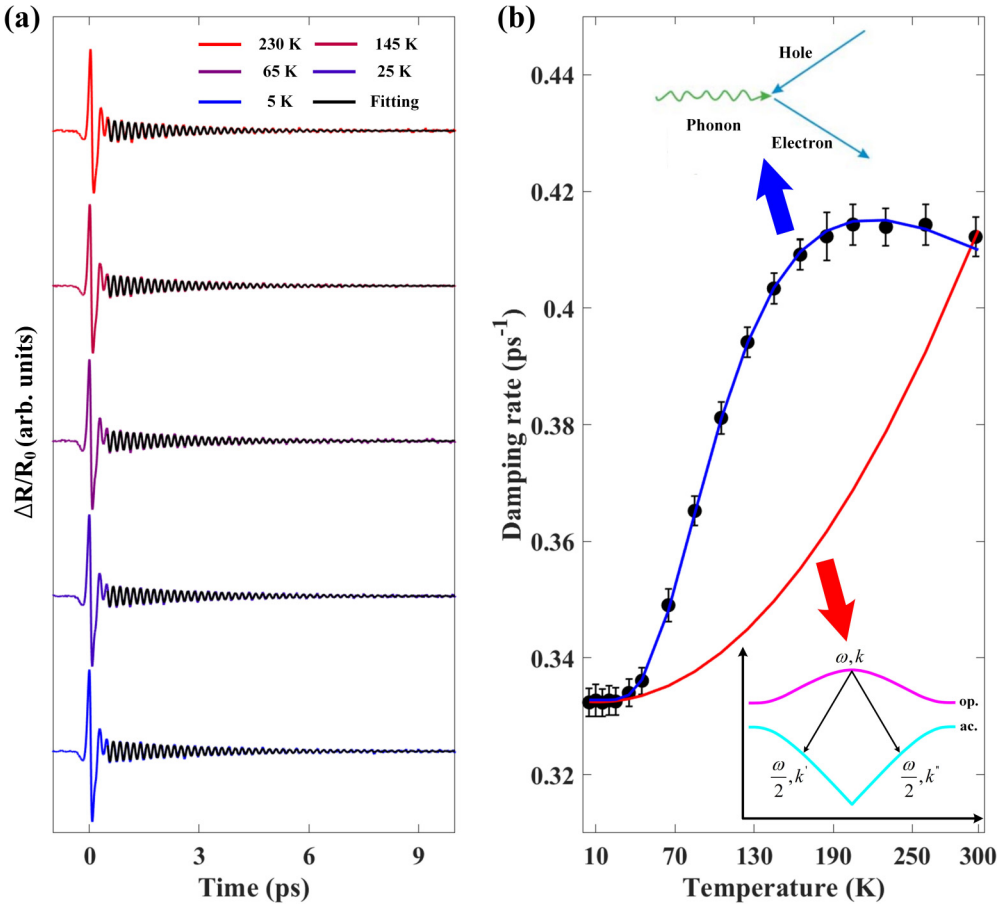

FIG. 2. Temperature-dependent phonon damping rates in β-WP_2. (a) The coherent phonon spectra at various temperatures, which are fitted by a linear combination of multiple damped harmonic oscillators (the black curves). (b) The extracted phonon damping rate of $A_1^{(1)}$ mode as a function of temperature (black circles). The blue curve is fitted by the optical phonons' decay into *e-h* pairs model while the red curve is indicating the optical phonons' decay into acoustic phonons scenario.

the nonequilibrium measurements is possibly due to the weak phonon amplitude [32] or relatively fast phonon damping rates [21], leading to high-frequency modulations from the lattice embedded in the noise background. Please note that at lower temperatures with weaker thermal atomic motions [33], other high-order A_1 phonon modes can be detected (please see the FT spectrum at 5 K in Appendix A).

It is well established that phonon damping rates only contain information related to available decay paths [34] while phonon energies/amplitudes involve multiple effects (e.g., lattice expansion or anharmonic renormalization) [17]; we hence begin the dynamic investigation of phonon scattering in β-WP_2 by analyzing the temperature-dependent damping rates. As shown in Fig. 2(a), the temporal oscillations are fitted with a linear combination of multiple exponentially decaying sinusoidal functions [28,32] (see Appendix B for the fitting procedure). It is worth mentioning that there exists a discrepancy between the experimental data and the theoretical fit at very early time delays, which indicates a transient Fano resonance [21] and will be discussed later. The extracted temperature-dependent damping rates of $A_1^{(1)}$ are plotted in Fig. 2(b). Here we focus on the $A_1^{(1)}$ mode due to low fitting uncertainties and the $A_1^{(2)}$ mode displays a similar damping rate behavior, which is presented in Appendix C. Interestingly, the $A_1^{(1)}$ damping rate exhibits an anomalous T-dependent trend: at temperatures below ~50 K, the damping rate of ~0.33 ps^{-1} maintains nearly constant. Then at the intermediate temperature range (50 K $< T <$ 180 K), the damping rate grows rapidly up to ~0.41 ps^{-1}, followed by a slight decrease as the temperature further increases. This type of behavior is distinct from that predicted by optical phonons decaying into acoustic phonons [as depicted in the bottom inset of Fig. 2(b)]. Such a three-phonon process is mathematically described by the cubic term of the anharmonic Hamiltonian (even higher anharmonic terms are also possible but much less likely) and the Bose-Einstein distribution of phonon populations will result in a monotonical, positive-curvature increase of damping rate with higher temperatures [the red curve in Fig. 2(b)] [35,36].

To understand this peculiar T-dependent behavior, we try to fit the damping rate by assuming that optical phonons decay into electron-hole (*e-h*) pairs. In this *e-h* creation process, an optical phonon with wave vector Π can excite an initial electronic state $|\Psi i\rangle$ with a wave vector Ψ into the

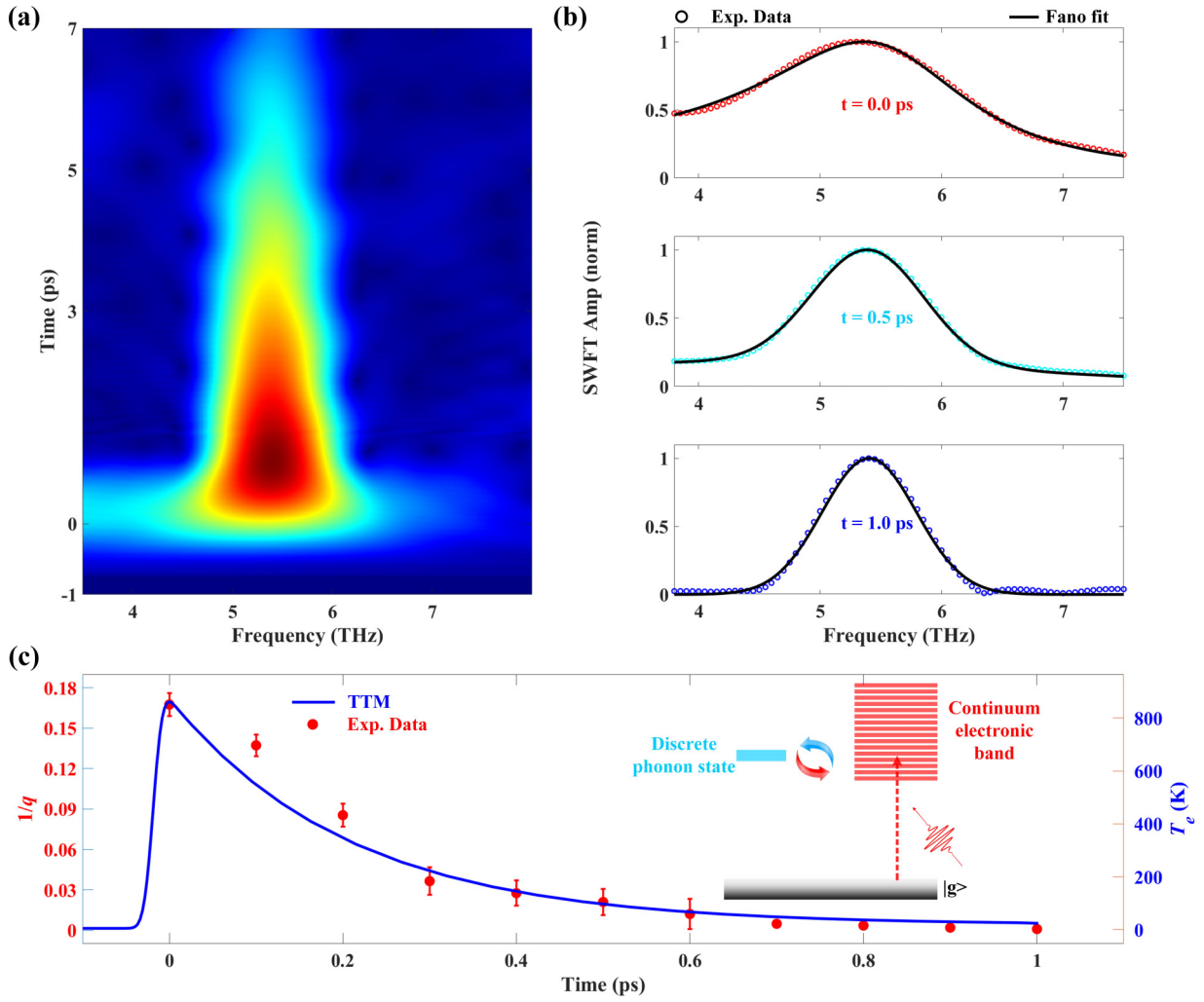

FIG. 3. Transient Fano resonance in β-WP_2 at room temperature. (a) The coherent phonon spectrum in the time and frequency domain obtained via the SWFT analysis. (b) Representative phonon spectra profiles at various delay times, where the solid lines present fittings with the Fano function. (c) Time dependence of the Fano parameter ($1/q$). The blue curve is the simulated electronic temperature based on a two-temperature model (TTM). The insert represents the Fano coupling mechanism in β-WP_2.

final electronic state $|(\Psi + \Pi)j\rangle$ and the phonon damping rate (i.e., the scattering probability γ) thus can be expressed by the Fermi (instead of Bose) functions at temperature T [17,20,37]: $\gamma(T) \propto f(\omega_a, T) - f(\omega_a + \omega_{\rm ph}, T)$, where f is the Fermi function, $\omega_{\rm ph}$ is the energy of the $A_1^{(1)}$ optical phonon mode, and ω_a denotes the energy distance between the initial electronic state and the Fermi energy. Please note that this model is entirely phenomenological, which can be satisfied only if the phonon-electron scatterings overwhelm phonon-phonon scatterings [37]. This model can produce a nonmonotonic T-dependent trend since the empty initial state at low temperatures renders the phonon-electron scattering less chance to occur while the thermally populated initial state at high temperatures greatly enhances the phonons' decay into e-h pairs process, which thus yields a nice fitting for the experimental results [see the blue curve in Fig. 2(b); the detailed fitting procedure is provided in Appendix C]. This agreement implies that momentum lost to phonons can return to fermions in β-WP_2 [17,38], which may account for the ultrahigh electron mobility.

As mentioned above, there possibly exists a transient Fano resonance in coherent phonon spectra according to the fitting discrepancy shown in Fig. 2(a). To confirm this scenario, sliding window Fourier transformation (SWFT) is utilized to obtain the time-frequency chronogram [21,29,39] from the time-domain data presented in Fig. 1(c) after subtracting the incoherent part (see details in Appendix D). As shown in Fig. 3(a), the $A_1^{(1)}$ phonon spectrum displays an antisymmetric line shape on the lower frequency side upon photoexcitation, which then gradually changes into a symmetric peak when the delay time is larger than ~1 ps. It is well known that, in the absence of large coupling strength between phonons and electrons, the phonon exhibits a symmetric line shape that can be described by a Lorentz oscillator [28,39]. In contrast, according to the many-body time-dependent model proposed by Hase and co-workers [21,40], an asymmetric Fano-like phonon line shape can be regarded as the coherent energy exchange between the optical phonon and electron-hole pair continuum considering the quantum interference nature of Fano resonance. Therefore, we argue that the observed

asymmetric line shape of the $A_1^{(1)}$ phonon mode provides another unequivocal signature of the "phonons' decay into e-h pairs" process in β-WP_2, and more interestingly, the asymmetry diminishes in a relatively short time range, suggesting that the coupling-induced Fano resonance in β-WP_2 is highly dependent on nonequilibrium dynamics of electrons (the $A_1^{(1)}$ phonon lifetime of > 2.5 ps is incongruent with the vanished time scale).

Since the vanished time scale of Fano resonance is largely consistent with the time scale when the electronic distribution is nonthermal as observed in other Weyl semimetals (i.e., 400–1200 fs) [41,42], we speculate that the transient behavior of Fano resonance may be dominated by the coherence loss of the continuumlike electrons during the thermal equilibrium establishment process between electronic and lattice subsystems. To test this hypothesis, we have fitted the experimental SWFT phonon spectra with the Fano line shape [20,21]: $I(\omega) = \frac{[q+(\omega-\omega_0)/\gamma]^2}{1+(\omega-\omega_0)^2/\gamma^2}$, where q is the Fano parameter, characterizing the specific asymmetric profile of the Fano response function (i.e., $1/q = 0$ indicates a perfect Lorentzian line shape); ω_0 and γ correspond to the resonance frequency and linewidth of the phonon, respectively. Fitting results based on the Fano line shape are shown in Fig. 3(b) with a frequency range 3.8–7.5 THz and in Fig. 9 with a wider frequency range (i.e., 0.5–7.5 THz). Meanwhile, we have also calculated the nonequilibrium electronic temperature in β-WP_2 upon photoexcitation using the two-temperature model [43] (details of the calculation are provided in Appendix E). These results are depicted in Fig. 3(c) as a function of the delay time and it can be found that the two-temperature model (the blue curve) predicts the time dependence of $1/q$ (the red circles) in a very good manner.

This agreement encourages us to interpret the transient Fano resonance as follows [see the inset in Fig. 3(c)]: Upon laser excitation, the displacive photogenerated coherent optical phonon (the $A_1^{(1)}$ mode) is strongly coupled with the photoexcited electrons through decaying into or being generated from the continuumlike conduction band electronic states [40,44], resulting in a Fano-like asymmetric phonon line shape. During this mutual energy and momentum exchange process, the photoexcited electrons gradually lost coherence (i.e., electrons dephase within 1 ps) in the electron-phonon thermalization process via the coherent emission of optical phonons or collision with ions, which finally causes the suppression of the Fano resonance. Please note that this transient Fano behavior is temperature independent (see the Fano analysis of SWFT data at other temperatures in Appendix D), which further supports that the transient Fano coupling is dominated by the electronic dephasing rather than the thermal populated electronic state occupation [20,44]. Moreover, it is worth mentioning that we have excluded the possibility that the Fano resonance is coming from the coupling between Weyl fermions and phonons, as recently reported in Weyl semimetal TaAs [20]. In β-WP_2, the Weyl nodes are located hundreds of meV below the Fermi surface [6], these Weyl points hence are less likely to interact with the displacive photogenerated coherent phonons with the energy scale of several tens meV.

To further support the experimental observation of phonons' decay into e-h pairs in β-WP_2, we turn to first-principles calculations to illustrate the possible scattering pathway of low-energy coherent phonon modes (calculation details are presented in Appendix F). Figure 4(a) shows the calculated phonon band structure with the phonon density of states (DOS). Consistent with previous calculations [17,34], there are three acoustic branches (0–4 THz) with very narrow bandwidth lying closer to one another. As previously discussed in boron arsenide [43], the bunching of three sharp acoustic branches restricts the phase space for decaying into acoustic phonons and makes the momentum conservation of three-phonon scatterings difficult to satisfy. Besides the reduced phase space, there is a relatively small amount of phonon DOS below ~5.2 THz, which also decreases the possibility of low-energy optical phonons decaying into acoustic phonons [17,34]. These two features in β-WP_2 lead to a prolonged phonon-phonon scattering lifetime and allows phonon-electron scattering processes to dominate the conventional phonon-phonon decay. The bunching and DOS arguments can also be quantitatively visualized by calculating phonon-phonon ($\tau_{\text{ph-ph}}$) and phonon-electron ($\tau_{\text{ph-}e}$) scattering lifetimes. As shown in Fig. 4(b), we have evaluated $\tau_{\text{ph-ph}}$ at high (300 K) and low (50 K) temperatures by using the PHONO3PY and VASP software packages [45]. For the $A_1^{(1)}$ optical phonons with a frequency of ~5 THz, the median $\tau_{\text{ph-ph}}$ at room temperature is about ~24 ps while this value increases to ~930 ps at 50 K due to the smaller amplitude of lattice atomic vibration and weaker anharmonicity [33]. For comparison, the temperature-dependent phonon-electron lifetimes for the same modes are estimated following the first-principles density-functional theory [34] [see Fig. 4(c),] which presents a $\tau_{\text{ph-ph}}$ / $\tau_{\text{ph-}e}$ ratio at least larger than 10 ($\tau_{\text{ph-ph}}$ / $\tau_{\text{ph-}e}$ goes to beyond 30 at 50 K). This magnitude of lifetime difference strongly suggests that phonons are likely to scatter much more frequently with electrons instead of phonons in β-WP_2. Please note that the calculated phonon lifetime is separated from experimental data in Fig. 2(b) at low temperatures, which is likely due to lacking consideration for defects/boundary scatterings in an idealized electronic structure calculation.

Altogether, our works experimentally evaluate the nonequilibrium phonon scattering process in β-WP_2, providing direct and unambiguous evidence to validate the dominant phonon-electron scattering process as previously suggested in the computational work. More importantly, in conjunction with first-principles calculations, our results put the seemingly unrelated hydrodynamic electron transport and Wiedemann-Franz deviated thermal transport into the same unified microscopic physical picture: as a result of the anomalous phonon-electron scattering process, electrons and phonons may become coupled, forming quasiparticles that lead to exotic transport properties [46]. Meanwhile, it would be very interesting to look for such dominant phonon-electron scattering in other heavy-atom-containing semimetals, which may provide unique insight into the phonon-mediated electron correlation phenomena (e.g., charge density waves or superconductivity) and offer a possible route to engineer these exotic quantum properties at high temperature.

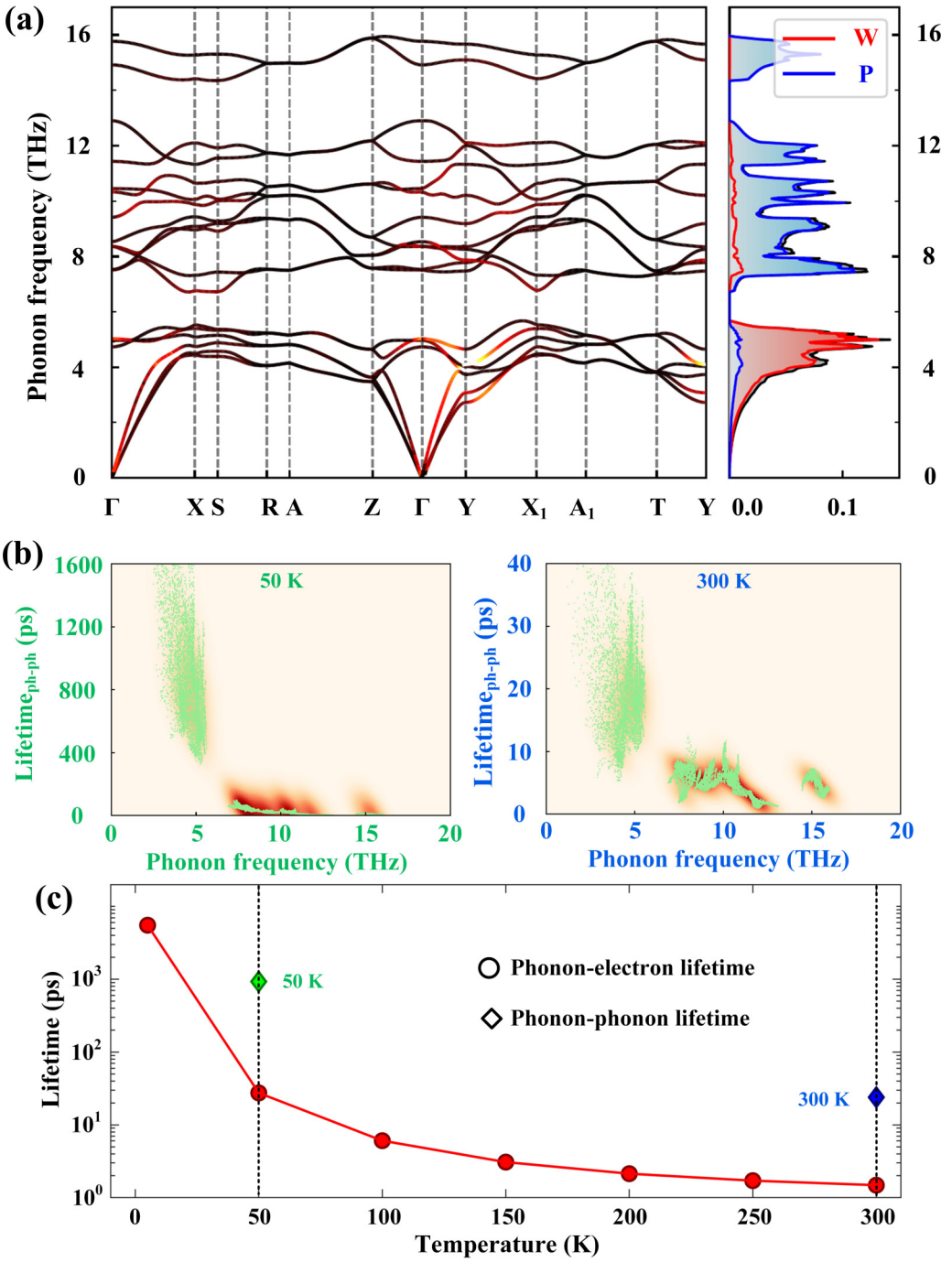

FIG. 4. First-principles calculations to illustrate the phonon scattering in β-WP_2. (a) Calculated phonon dispersion for the orthorhombic β-WP_2 structure with the phonon densities of states. (b) Calculated phonon-phonon scattering lifetime in β-WP_2 at 50 K (the left panel) and 300 K (the right panel) using PHONO3PY and VASP software packages [43]. (c) Calculated temperature-dependent phonon-electron scattering lifetime in β-WP_2 using the first-principles density-functional theory [34]. The calculated median lifetimes of phonon-phonon scatterings are also presented for comparison.

III. CONCLUSIONS

In summary, we have performed ultrafast coherent phonon spectroscopy to investigate the dynamical phonon scattering processes in β-WP_2. Compelling evidence for dominating scattering of optical phonons by electrons has been found through the observation of an anomalous temperature-dependent phonon damping rate and the transient Fano line shape of phonon spectra. Our nonequilibrium spectroscopy studies, combined with the first-principle calculations on the phonon dispersion/lifetime, provide insight into previous Raman experiments that were restricted under equilibrium conditions and may enhance current understandings of the link between phonon-related scatterings and anomalous transport properties in WP_2.

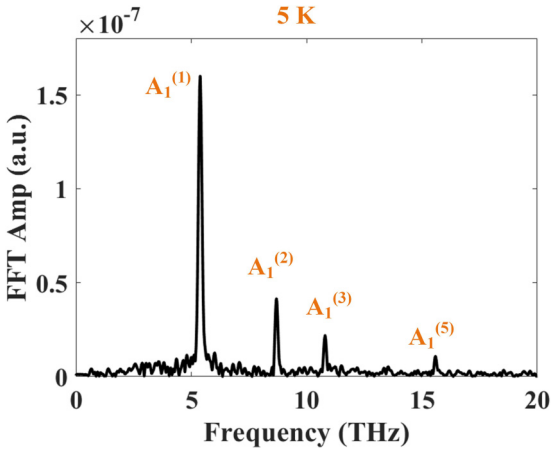

FIG. 5. FT spectrum of the time-domain lattice vibrations at 5 K showing other high-order A_1 phonon modes.

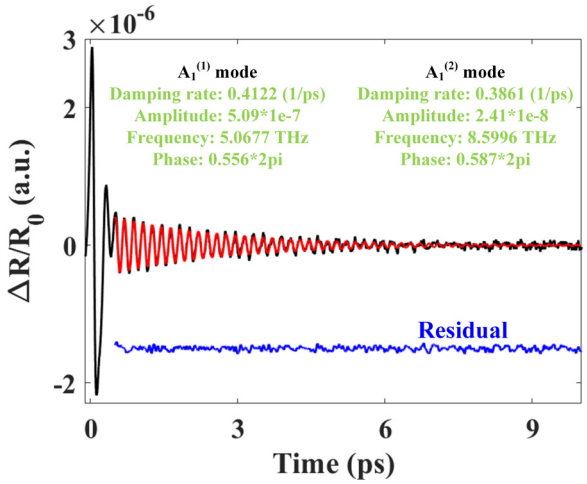

FIG. 6. Oscillatory time-domain data at RT and numerical fitting based on the damped harmonic oscillator model. The residual is offset for clarity.

ACKNOWLEDGMENTS

This work was supported by Science Challenge Project (Grant No. TZ2018001), National Natural Science Foundation of China (Grants No. 11872058 and No. 51902152), and Project of State Key Laboratory of Environment-friendly Energy Materials, Southwest University of Science and Technology (20fksy06).

APPENDIX A: FEMTOSECOND-RESOLVED COHERENT PHONON SPECTROSCOPY

Besides the description in the main text, other experimental details of coherent phonon spectroscopy are provided here. The reflected probe pulse from the SnSe sample is fed into a polarization beam splitter. The parallel ($\Delta R_\parallel$) and perpendicular ($\Delta R_\perp$) polarized portion of the reflected probe pulse is monitored with balanced photodiodes (PD1 and PD2). The differential reflectivity is calculated using $\frac{\Delta R}{R_0} = \frac{\Delta R_\parallel - \Delta R_\perp}{R_0}$ to cancel the common mode noise and then amplified with a current amplifier and averaged in a digital oscilloscope. To filter the nonoscillatory background in the temporal evolution, a bandpass filter (3–300 kHz) was used to amplify the measurements (see Fig. 5).

APPENDIX B: FITTING THE OSCILLATORY TIME-DOMAIN DATA

To analyze the T-dependent damping rate of the coherent phonon modes, we have fitted the time-domain oscillation signals with the damped harmonic oscillator model [28–31]:

$$\frac{\Delta R(t)}{R} = A \times \exp(-t \times \gamma_{\rm ph}) \cos(\omega_{\rm ph} t + \varphi_{\rm ph}) + C, \quad \text{(B1)}$$

where A, $\gamma_{\rm ph}$, $\omega_{\rm ph}$, and $\varphi_{\rm ph}$ are the amplitude, the damping rate, the frequency, and the initial phase of the coherent phonon mode, respectively, and C is a constant background.

In the fitting process, we first fit the mode that has the strongest amplitude (i.e., the $A_1^{(1)}$ mode), then subtract the resulting fit from the raw data, and perform the same routine on the residual signal to extract the data on the next most intense mode.

As shown in Fig. 6, using the room temperature (RT) time domain data as an example, the oscillation signal can be well fitted for later delay times (i.e., $\Delta t > 1$ ps). In fact, there is a significant phase shift of the coherent phonon at the early time delays (i.e., $\Delta t < 1$ ps), which cannot be modeled by a simple damped oscillator. This discrepancy, observed only at early time delays, is ascribed to a coherent correlation between the phonon and the photogenerated excitation, as detailed in Fig. 3.

APPENDIX C: T-DEPENDENT DAMPING RATE OF COHERENT PHONONS

According to the discussion in Fig. 2, we can model the T-dependent damping rate of coherent phonons by assuming that they are decaying into electron-hole (e-h) pairs. As detailed previously [17], if considering a system with a null electron gap, the phonon damping rate or the phonon linewidth can be expressed by Fermi-Dirac functions (Fermi energy $E_F = 0$), which takes the form

$$\gamma(T) = \gamma_0 \left[f\left(-\frac{\hbar\omega_{\rm ph}}{2k_B T}\right) - f\left(\frac{\hbar\omega_{\rm ph}}{2k_B T}\right) \right], \quad \text{(C1)}$$

where the first Fermi factor accounts for the initial electron state (hole), the second accounts for the final electron state, $\hbar\omega_{\rm ph}$ is the energy of the optical phonon, $f(x) = 1/[\exp(x) + 1]$ is the Fermi-Dirac distribution, and γ_0 is the zero-temperature damping rate.

If the Fermi energy is nonzero, the above expression should be modified as

$$\gamma(T) = \gamma_0 \left[f\left(-\frac{\hbar\omega_{\rm ph}}{2k_B T} + \frac{E_F}{k_B T}\right) - f\left(\frac{\hbar\omega_{\rm ph}}{2k_B T} - \frac{E_F}{k_B T}\right) \right]. \quad \text{(C2)}$$

While considering the nearly parallel spin-orbit split bands of β-WP_2 and refering to the inter-/intraband transitions produced by the decay of an optical phonon (see Figs. 7), we can

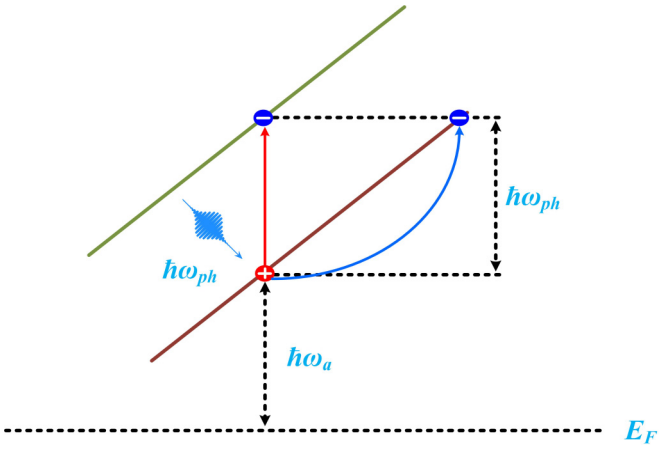

FIG. 7. Schematic illustrating the interband and the intraband electron transitions excited by optical phonons.

further modify the expression as follows:

$$\gamma(T) = A + \gamma_0\left[f\left(\frac{\hbar\omega_a}{k_BT}\right) - f\left(\frac{\hbar\omega_{\rm ph} + \hbar\omega_a}{k_BT}\right)\right], \quad \text{(C3)}$$

where A is a temperature-independent term that accounts for any anharmonic renormalization and $\hbar\omega_a$ is the energy distance between E_F and the initial state of the electron.

Using this model, the T-dependent damping rate of $A_1^{(1)}$ and $A_1^{(2)}$ (see Fig. 8) modes can be well-reproduced with the fitting parameters shown in Table I.

APPENDIX D: SLIDING WINDOW FOURIER TRANSFORMATION

Consistent with previous transient Fano analysis in coherent phonon spectroscopy, we utilize the sliding window Fourier transform (SWFT) with smoothed-pseudo-Wigner-Ville functions to extract time-dependent spectral profiles of coherent phonons (see Figs. 9 and 10). SWFT is operated based on the fact that a frequency-dependent power spectrum, $S(\omega)^2$, can be expressed as the Fourier transform of the time-dependent signal, $R(t)$:

$$|S(w)|^2 = \int dt R(t)\, e^{-iwt}. \quad \text{(D1)}$$

Here, $R(t)$ is obtained by scanning across the experimental time-dependent oscillatory pattern with a Hann window function. Therefore, the frequency resolution of this method is mainly determined by the width (τ) of the selected window function (e.g., a narrower width means higher frequency resolution but massive computer calculations), while in our case, we have tested different τ values and found that τ= 500 fs is precise enough to obtain an optimized frequency resolution.

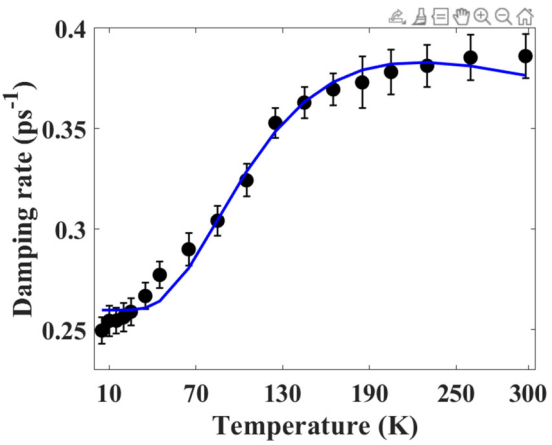

FIG. 8. The extracted phonon damping rate of $A_1^{(2)}$ mode as a function of temperature (black circles). The blue curve is fitted by the optical phonons' decay into e-ph pairs model.

TABLE I. Fitting parameters for $A_1^{(1)}$ and $A_1^{(2)}$ modes with the optical phonons' decay into e-ph pairs model.

Mode	A (1/ps)	γ_0 (1/ps)	ω_a (THz)
$A_1^{(1)}$	0.3328	0.4978	4.6453
$A_1^{(2)}$	0.2597	0.7626	4.8117

APPENDIX E: TWO-TEMPERATURE MODEL

To further understand the transient Fano resonance (i.e., the $1/q$ value), we have utilized the two-temperature model (TTM) to describe the thermalization process between the lattice temperature T_l and the electron temperature T_e [47]:

$$\begin{aligned} C_e\frac{\partial T_e}{\partial t} &= -g(T_e - T_l) + P(t), \\ C_l\frac{\partial T_l}{\partial t} &= g(T_e - T_l), \end{aligned} \quad \text{(E1)}$$

where T_e and T_l are the temperatures of the electrons and the lattice, respectively. C_e and C_l are the heat capacity of the electron and the lattice, respectively. The temperature-dependent heat capacity of electrons is determined by $C_e = \frac{\pi^2}{2}Nk_{\rm B}^2\frac{T}{E_F}$ ($k_{\rm B}$ is the Boltzmann constant and N is the electron density per mole; E_F is the Fermi energy) [5], while the lattice heat capacity is determined via $C_l = C$–C_e (the temperature-dependent heat capacity C is taken from Ref. [6]). g is the electron-phonon coupling constant which gives the relation between the heating of the electrons and the lattice (this will be an adjustable fitting parameter). The final term $P(t)$ in the first equation is the source term of the laser pulse that heats the sample. The laser pulse can be written as the Gaussian function:

$$P(t) = F\alpha\frac{2\sqrt{\ln 2}}{\tau_{\rm FWHM}\sqrt{\pi}}e^{-4\ln 2(t^2/\tau_{\rm FWHM}^2)}, \quad \text{(E2)}$$

where F is the pump fluence, α is the absorption coefficient, and $\tau_{\rm FWHM}$ is the full width at half maximum of the laser pulse (~20 fs).

Therefore, taking the environment temperature of 298 K and the pump fluence of 5 $\mu J/cm^2$, using the TTM with g as an adjustable parameter ($g = 1.34\times 10^{17}$ W/m^3/K, which is almost an order of magnitude larger than the value in simple metals [22]), we can extract the reliable electron and lattice

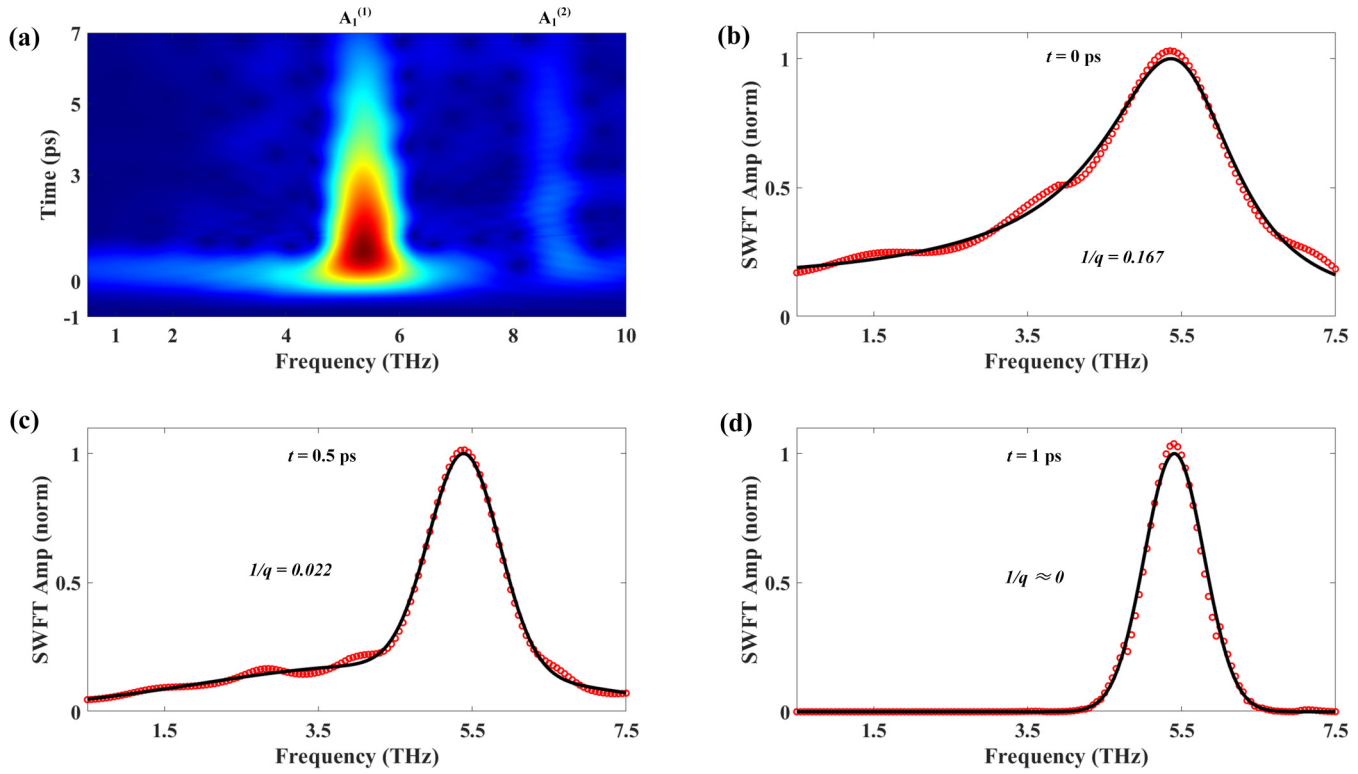

FIG. 9. SWFT in a broad frequency range. (a) The coherent phonon spectrum at room temperature in the time and frequency domain obtained via the SWFT analysis. In such a wider energy range, both $A_1^{(1)}$ and $A_1^{(2)}$ modes can be resolved. (b)–(d) Representative phonon spectra profiles at 0 ps (b), 0.5 ps (c), and 1 ps (d). The extract q values are listed and the solid lines present fittings with the Fano function.

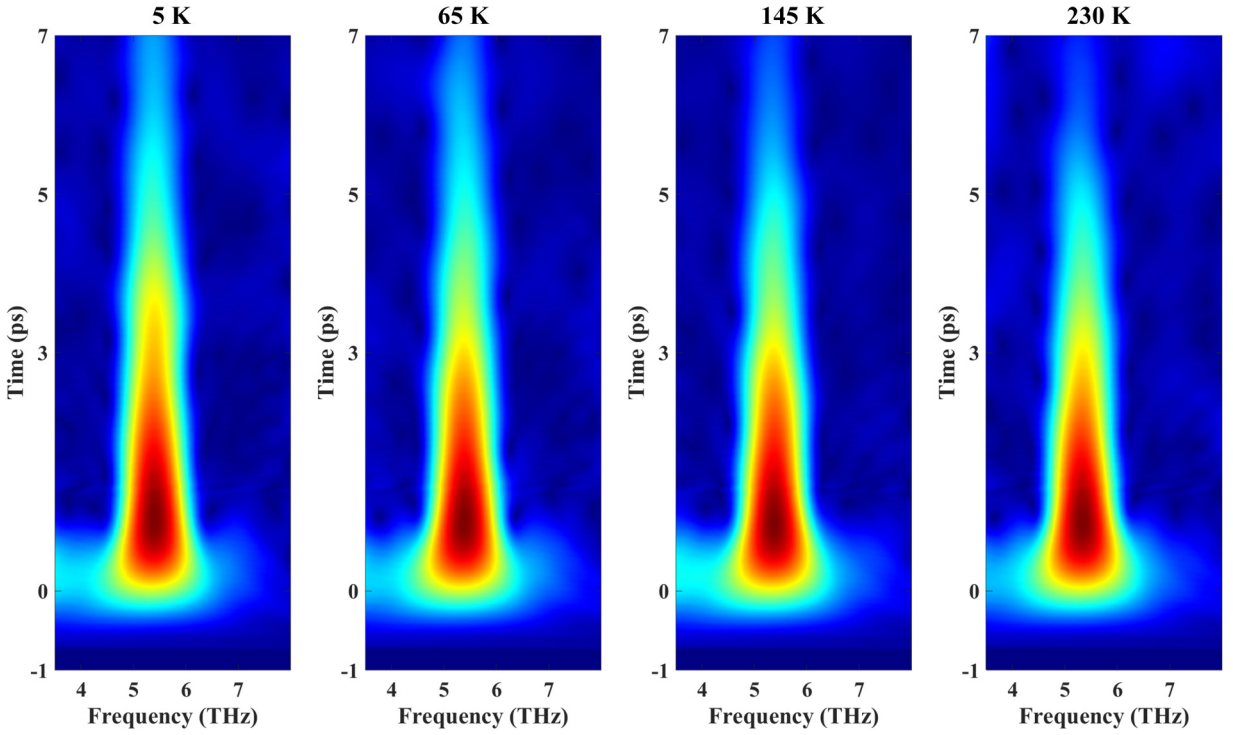

FIG. 10. The coherent phonon spectrum in the time and frequency domain obtained via the SWFT analysis at four different temperatures, which shows a T-independent transient Fano resonance.

temperatures depending on an accurate fitting of the time-dependent $1/q$.

APPENDIX F: FIRST-PRINCIPLES CALCULATIONS

First-principles calculations were performed based on the density functional theory (DFT), as implemented in the QUANTUM ESPRESSO package [48,49]. The exchange-correlation functional is treated with the generalized gradient approximation using the Perdew-Burke-Ernzerhof (PBE) realization [50]. The ultrasoft pseudopotentials are adopted. We considered 14 electrons for W ($5s^2\,5p^6\,5d^4\,6d^2$), and 5 electrons for P ($3s^2\,3p^3$) as valence electrons. Spin-orbit coupling effects were included in the calculation. The kinetic energy cutoff for the wave functions was set to 60 Ry, while for the charge density it was fixed to 600 Ry. For the self-consistent calculations, the Brillouin zone integration was performed on grid mesh of $10 \times 10 \times 12$ k points for electronic band structure, and $5 \times 5 \times 6$ q points for phonon dispersion. The convergence criterion was set to 10^{-8} Ry. To calculate the electron-phonon coupling matrix elements of WP_2 with the electron-phonon WANNIER package [51,52], a Wannier tight-binding Hamiltonian consisting of W-6s, W-5d, P-3s, and P-3p orbitals was constructed.

For the thermal conductivity and phonon lifetime calculation, we employed PHONO3PY [53] and VASP [54,55] software packages. The projector-augmented wave (PAW) pseudopotentials were adopted in the calculation [56,57]. The generalized gradient approximation with the Perdew-Burke-Ernzerhof (PBE) realization was used for the exchange-correlation functional. The valence electrons treated in the calculations include W ($5d^4\,6s^2$) and P ($3s^2\,3p^3$). The kinetic energy cutoff was fixed to 400 eV. The third-order force constants were calculated using the $2 \times 2 \times 2$ supercell (48 atoms) with finite atomic displacements of 0.03 Å. The Brillouin zone (BZ) integration was performed on a Γ-centered mesh of $4 \times 4 \times 5$ k points. The energy convergence criteria were set to be 10^{-7} eV.

[1] N. P. Armitage, E. J. Mele, and A. Vishwanath, Weyl and Dirac semimetals in three-dimensional solids, Rev. Mod. Phys. **90**, 015001 (2018).

[2] C. Shekhar, A. K. Nayak, Y. Sun, M. Schmidt, M. Nicklas, I. Leermakers, U. Zeitler, Y. Skourski, J. Wosnitza, Z. Liu, Y. Chen, W. Schnelle, H. Borrmann, Y. Grin, C. Felser, and B. Yan, Extremely large magnetoresistance and ultrahigh mobility in the topological Weyl semimetal candidate NbP, Nat. Phys. **11**, 645 (2015).

[3] X. Huang, L. Zhao, Y. Long, P. Wang, D. Chen, Z. Yang, H. Liang, M. Xue, H. Weng, and Z. Fang, Observation of the Chiral-Anomaly-Induced Negative Magnetoresistance in 3D Weyl Semimetal TaAs, Phys. Rev. X **5**, 031023 (2015).

[4] A. Soluyanov, D.Gresch, Z. Wang, Q. Wu, M. Troyer, X. Dai, and B. A. Bernevig, Type-II Weyl semimetals, Nature (London) **527**, 495 (2015).

[5] J. Liu, F. Xia, D. Xiao, F. J. García de Abajo, and D. Sun, Semimetals for high-performance photodetection, Nat. Mater. **19**, 830 (2020).

[6] G. Autès, D. Gresch, M. Troyer, A. A. Soluyanov, and O. V. Yazyev, Robust Type-II Weyl Semimetal Phase in Transition Metal Diphosphides Xp_2(X = Mo, W), Phys. Rev. Lett. **117**, 066402 (2016).

[7] R. Schönemann, N. Aryal, Q. Zhou, Y.-C. Chiu, K.-W. Chen, T. J. Martin, G. T. McCandless, J. Y. Chan, E. Manousakis, and L. Balicas, Fermi surface of the Weyl Type-II metallic candidate WP_2, Phys. Rev. B **96**, 121108(R) (2017).

[8] E. Razzoli, B. Zwartsenberg, M. Michiardi, F. Boschini, R. P. Day, I. S. Elfimov, J. D. Denlinger, V. Süss, C. Felser, and A. Damascelli, Stable Weyl points, trivial surface states, and particle-hole compensation in WP_2, Phys. Rev. B **97**, 201103(R) (2018).

[9] J. Gooth, F. Menges, N. Kumar, V. Süβ, C. Shekhar, Y. Sun, U. Drechsler, R. Zierold, C. Felser, and B. Gotsmann, Thermal and electrical signatures of a hydrodynamic electron fluid in tungsten diphosphide, Nat. Commun. **9**, 4093 (2018).

[10] A. Jaoui *et al.*, Departure from the wiedemann–franz law in WP_2 driven by mismatch in T-square resistivity prefactors, npj Quantum Mater. **3**, 64 (2018).

[11] M. R. van Delft *et al.*, Sondheimer oscillations as a probe of non-ohmic flow in WP_2 crystals, Nat. Commun. **12**, 4799 (2021).

[12] E. S. Toberer, L. L. Baranowski, and C. Dames, Advances in thermal conductivity, Annu. Rev. Mater. Res. **42**, 179 (2012).

[13] X. Qian, J. Zhou, and G. Chen, Phonon-engineered extreme thermal conductivity materials, Nat. Mater. **20**, 1188 (2021).

[14] J. Yu, Y. Han, H. Zhang, X. Ding, L. Qiao, and J. Hu, Excimer formation in the Non-Van-Der-Waals 2D semiconductor Bi_2O_2Se, Adv. Mater. **34**, 2204227 (2022).

[15] J. Coulter, R. Sundararaman, and P. Narang, Microscopic origins of hydrodynamic transport in the type-II Weyl semimetal WP_2, Phys. Rev. B **98**, 115130(R) (2018).

[16] B. Su, Y. Song, Y. Hou, X. Chen, J. Zhao, Y. Ma, Y. Yang, J. Guo, J. Luo, and Z. Chen, Strong and tunable electrical anisotropy in Type-II Weyl semimetal candidate WP_2 with broken inversion symmetry, Adv. Mater. **31**, 1903498 (2019).

[17] G. B. Osterhoudt, Y. Wang, C. A. C. Garcia, V. M. Plisson, J. Gooth, C. Felser, P. Narang, and K. S. Burch, Evidence for Dominant Phonon-Electron Scattering in Weyl Semimetal WP_2, Phys. Rev. X **11**, 011017 (2021).

[18] D. Wulferding, P. Lemmens, F. Büscher, D. Schmeltzer, C. Felser, and C. Shekhar, Effect of topology on quasiparticle interactions in the Weyl semimetal WP_2, Phys. Rev. B **102**, 075116 (2020).

[19] M. Hase, M. Kitajima, S. I. Nakashima, and K. Mizoguchi, Dynamics of Coherent Anharmonic Phonons in Bismuth Using High Density Photoexcitation, Phys. Rev. Lett. **88**, 067401 (2002).

[20] B. Xu *et al.*, Temperature-tunable fano resonance induced by strong coupling between Weyl fermions and phonons in TaAs, Nat. Commun. **8**, 14933 (2017).

[21] M. Hase, J. Demsar, and M. Kitajima, Photoinduced fano resonance of coherent phonons in zinc, Phys. Rev. B **74**, 212301 (2006).

[22] M.-Y. Yao *et al.*, Observation of Weyl Nodes in Robust Type-II Weyl Semimetal WP_2, Phys. Rev. Lett. **122**, 176402 (2019).

[23] Y.-Y. Lv *et al.*, High-harmonic generation in Weyl semimetal β-WP_2 crystals, Nat. Commun. **12**, 6437 (2021).

[24] N. Kumar *et al.*, Extremely high magnetoresistance and conductivity in the type-II Weyl semimetals WP_2 and MoP_2, Nat. Commun. **8**, 1642 (2017).

[25] E. Kroumova, M. I. Aroyo, J. M. Perez-Mato, A. Kirov, C. Capillas, S. Ivantchev, and H. Wondratschek, Bilbao crystallographic server: Useful databases and tools for phase-transition studies, Phase Transitions **76**, 155 (2003).

[26] R. R. Alfano and S. L. Shapiro, Optical Phonon Lifetime Measured Directly with Picosecond Pulses, Phys. Rev. Lett. **26**, 1247 (1971).

[27] Y. Han *et al.*, Photoinduced ultrafast symmetry switch in SnSe, J. Phys. Chem. Lett. **13**, 442 (2022).

[28] L. Wang, Y. Han, J. Yu, F. Xu, H. Zhang, C. Gong, H. Lei, and J. Hu, Absence of Kondo effect in $CeNiGe_3$ revealed by coherent phonon dynamics, Phys. Rev. B **104**, 205133 (2021).

[29] J. Yu, Y. Han, L. Wang, F. Xu, H. Zhang, Y. Yu, Q. Wu, and J. Hu, Visualizing nonlinear phononics in layered $ReSe_2$, J. Phys. Chem. Lett. **12**, 5178 (2021).

[30] J. Yu, Y. Han, H. Zhang, O. V. Misochko, K. G. Nakamura, and J. Hu, Attosecond-resolved coherent control of lattice vibrations in thermoelectric SnSe, J. Phys. Chem. Lett. **13**, 2584 (2022).

[31] O. V. Misochko, J. Flock, and T. Dekorsy, Polarization dependence of coherent phonon generation and detection in the three-dimensional topological insulator Bi_2Te_3, Phys. Rev. B **91**, 174303 (2015).

[32] T. Y. Jeong *et al.*, Coherent lattice vibrations in mono- and few-layer WSe_2, ACS Nano **10**, 5560 (2016).

[33] Y. Guo, M. Bescond, Z. Zhang, M. Luisier, M. Nomura, and S. Volz, Quantum mechanical modeling of anharmonic phonon-phonon scattering in nanostructures, Phys. Rev. B **102**, 195412 (2020).

[34] J. Coulter, G. B. Osterhoudt, C. A. C. Garcia, Y. Wang, V. M. Plisson, B. Shen, N. Ni, K. S. Burch, and P. Narang, Uncovering electron-phonon scattering and phonon dynamics in Type-I Weyl semimetals, Phys. Rev. B **100**, 220301(R) (2019).

[35] P. G. Klemens, Anharmonic decay of optical phonons, Phys. Rev. **148**, 845 (1966).

[36] N. Bonini, M. Lazzeri, N. Marzari, and F. Mauri, Phonon Anharmonicities in Graphite and Graphene, Phys. Rev. Lett. **99**, 176802 (2007).

[37] H.-Y. Yang *et al.*, Evidence of a coupled electron-phonon liquid in $NbGe_2$, Nat. Commun. **12**, 5292 (2021).

[38] G. Varnavides, A. S. Jermyn, P. Anikeeva, C. Felser, and P. Narang, Electron hydrodynamics in anisotropic materials, Nat. Commun. **11**, 4710 (2020).

[39] J. Yu, S. Hu, H. Gao, S. Delikanli, B. Liu, J. J. Jasieniak, M. Sharma, and H. V. Demir, Observation of phonon cascades in Cu-doped colloidal quantum wells, Nano Lett. **22**, 10224 (2022).

[40] M. Hase, M. Kitajima, A. M. Constantinescu, and H. Petek, The birth of a quasiparticle in silicon observed in time–frequency space, Nature (London) **426**, 51 (2003).

[41] E. J. Sie *et al.*, An ultrafast symmetry switch in a Weyl semimetal, Nature (London) **565**, 61 (2019).

[42] Q. Wu, F. Sun, Q. Zhang, L. X. Zhao, G.-F. Chen, and J. Zhao, Quasiparticle dynamics and electron-phonon coupling in Weyl semimetal TaAs, Phys. Rev. Mater. **4**, 064201 (2020).

[43] A. Togo and I. Tanaka, First principles phonon calculations in materials science, Scr. Mater. **108**, 1 (2015).

[44] R. Mondal, A. Arai, Y. Saito, P. Fons, A. V. Kolobov, J. Tominaga, and M. Hase, Coherent Dirac plasmons in topological insulators, Phys. Rev. B **97**, 144306 (2018).

[45] L. Lindsay, D. A. Broido, and T. L. Reinecke, First-Principles Determination Of Ultrahigh Thermal Conductivity Of Boron Arsenide: A Competitor for Diamond?, Phys. Rev. Lett. **111**, 025901 (2013).

[46] S. Chen, The role of phonons in a topological material, Physics **14**, s11 (2021).

[47] J. Yu, Y. Han, Q. Yin, Z. Nie, L. Wang, C. Gong, Z. Tu, F. Xu, Y. Liu, H. Zhang, O. V. Misochoko, S. Meng, H. Lei, and J. Hu, All-optical manipulation of charge density waves in kagome metal CsV_3Sb_5, Phys. Rev. B **107**, 174303 (2023).

[48] P. Giannozzi *et al.*, QUANTUM ESPRESSO: A Modular and open-source software project for quantum simulations of materials, J. Phys.: Condens. Matter **21**, 395502 (2009).

[49] P. Giannozzi *et al.*, Advanced capabilities for materials modelling with quantum ESPRESSO, J. Phys.: Condens. Matter **29**, 465901 (2017).

[50] J. P. Perdew, K. Burke, and M. Ernzerhof, Generalized Gradient Approximation Made Simple, Phys. Rev. Lett. **77**, 3865 (1996).

[51] S. Poncé, E. R. Margine, C. Verdi, and F. Giustino, EPW: Electron–phonon coupling, transport and superconducting properties using maximally localized wannier functions, Comput. Phys. Commun. **209**, 116 (2016).

[52] F. Giustino, M. L. Cohen, and S. G. Louie, Electron-phonon interaction using wannier functions, Phys. Rev. B **76**, 165108 (2007).

[53] A. Togo, L. Chaput, and I. Tanaka, Distributions of phonon lifetimes in brillouin zones, Phys. Rev. B **91**, 094306 (2015).

[54] G. Kresse and J. Furthmüller, Efficient iterative schemes for ab initio total-energy calculations using a plane-wave basis set, Phys. Rev. B **54**, 11169 (1996).

[55] G. Kresse and J. Furthmüller, Efficiency of ab-initio total energy calculations for metals and semiconductors using a plane-wave basis set, Comput. Mater. Sci. **6**, 15 (1996).

[56] P. E. Blöchl, Projector augmented-wave method, Phys. Rev. B **50**, 17953 (1994).

[57] G. Kresse and D. Joubert, From ultrasoft pseudopotentials to the projector augmented-wave method, Phys. Rev. B **59**, 1758 (1999).